

Directed Aggregation of Cellulose Nanocrystals to Enhance Chiral Twist

Kévin Ballu, Jia-Hui Lim, Thomas G. Parton, Richard M. Parker, Bruno Frka-Petesic, Alexei A. Lapkin, Yu Ogawa, Silvia Vignolini**

Kévin Ballu, Dr Richard M Parker, Dr Bruno Frka-Petesic
Yusuf Hamied Department of Chemistry, University of Cambridge, Cambridge CB2 1EW, United Kingdom

Jia-Hui Lim, Dr Yu Ogawa
Univ. Grenoble Alpes, CNRS, CERMAV, 38000 Grenoble, France
* E-mail: yu.ogawa@cermav.cnrs.fr

Dr Thomas G Parton, Prof Silvia Vignolini
Department of Sustainable and Bio-inspired Materials, Max Planck Institute of Colloids and Interfaces, 14476 Potsdam, Germany
* E-mail: sv@mpikg.mpg.de

Dr Bruno Frka-Petesic
International Institute for Sustainability with Knotted Chiral Meta Matter (WPI-SKCM²), Hiroshima University, Hiroshima 739-8526, Japan

Prof Alexei Lapkin
Department of Chemical Engineering and Biotechnology, Philippa Fawcett Drive, Cambridge CB3 0AS, United Kingdom

Prof Alexei Lapkin
Innovative Center in Digital Molecular Technologies, Yusuf Hamied Department of Chemistry, University of Cambridge, Cambridge CB2 1EW, United Kingdom

Keywords: cellulose nanocrystals, chirality, particle morphology, transmission electron microscopy, scanning nanobeam electron diffraction (SNBED)

Abstract

Cellulose nanocrystals (CNCs) are bioderived nanoparticles that can be isolated from any source of natural cellulose via sulfuric acid hydrolysis. Arising from a combination of the negatively-charged sulfate half-ester groups grafted during this process and their elongated morphology, CNCs typically form colloidal cholesteric liquid crystalline phases in aqueous suspension. Recently, the chiral strength of such a CNC mesophase was correlated to the presence of CNCs with a “bundle” morphology, analogous to the case of chiral dopants in molecular liquid crystal systems. This indicates the central role these composite particles play in the chiral behavior of CNCs, however the origin and formation pathway of the CNC bundles remains elusive. In this study, we systematically explore how different post-hydrolysis treatments alter the morphology of the CNCs (using electron microscopy, viscosimetry, and electron diffraction) and correlate this to changes in the observed liquid crystalline behavior. We found that the centrifugation step applied during CNC purification favors the formation of bundles of aligned crystallites, attached preferentially on their hydrophobic faces. This is in stark contrast to ionic treatments, where uncontrolled aggregation dominates. This reveals the importance of these often-disregarded purification steps on the final chiral and liquid crystalline properties of CNCs and promotes routes to tailor them towards a variety of applications.

1. Introduction

Cellulose nanocrystals (CNCs) are highly-crystalline bioderived colloidal nanoparticles that can be isolated from various types of cellulose sources.^[1,2] This class of nanomaterial has captured the attention of material scientists in different fields and for a wide range of promising applications.^[3] In particular, CNCs possess the fascinating ability to spontaneously organize in water to form a cholesteric (aka chiral nematic) liquid crystal phase, which upon solvent evaporation can result in the formation of dye-free, structurally colored films.^[2,4]

Unlike the synthesis of monodisperse nanoparticles (e.g. silica, gold), the extraction of CNCs from natural wood and cotton leads to morphologically diverse CNC suspensions, containing both individual crystallites as well as composite particles formed from multiple crystallites.^[5] Importantly, the presence of such composite particles leads to inconsistencies in the literature regarding what is considered an individual CNC.^[2] The needs for appropriate terminology is particularly evident in one of our recent studies that highlighted how the nanoscale morphology of individual CNCs regulates their chiral self-organization.^[6] In particular, we observed that the proportion of bundle-like CNCs (i.e., composite particles made from laterally associated crystallites) was correlated with a decrease in the cholesteric pitch and a narrowing of the biphasic regime.^[6] This indicated that the chiral behavior of CNCs could be manipulated simply by changing the morphology of the bundles without any other specific treatment of the suspension, and that the presence of this chiral subpopulation shared some analogy with the chiral dopants commonly used in molecular liquid crystal systems.

While many methods have been developed for the isolation of CNCs,^[7,8] studies focusing on their liquid crystalline behavior most commonly exploit their extraction route by sulfuric acid hydrolysis of cellulose, followed by various purification steps.^[7] At the laboratory scale, the purification usually consists of several rounds of centrifugation, allowing for the separation of the acidic supernatant from the pelletized CNCs, followed by dialysis in deionized water. The obtained colloidal CNC suspension is electrostatically stabilized by the negatively charged sulfate half-ester groups grafted to their surface during hydrolysis.^[9]

In this work, we investigate the impact of the post-hydrolysis purification process on the architecture of CNC bundles, and we complement this with the use of divalent ions to trigger irreversible aggregation of CNC particles. From transmission electron microscopy (TEM) and viscosity measurements, we show that the centrifugation step commonly used to purify CNCs favors the formation of the laterally aligned composite particles, which we call “bundles”. Scanning nanobeam electron diffraction (SNBED) shows that these bundles are preferentially associated through their hydrophobic faces, and comparative pitch measurements in suspension confirm that they exhibit enhanced chiral strength. Conversely, aggregation with calcium chloride (CaCl₂), with or without centrifugation, leads to an irreversible increase of the CNC size by forming randomly associated composite particles, which can be used to promote gelation at lower concentrations.

2. Results and Discussion

2.1 Preparation of CNC Suspensions

A CNC suspension was prepared from cotton cellulose by sulfuric acid hydrolysis according to the conditions summarized in **Figure 1a**, (detailed methodology can be found in the Experimental Section). The hydrolyzed mixture was quenched and split at each centrifugation step to obtain CNCs that were never centrifuged (**C0**) or centrifuged once (**C1**), twice (**C2**), or three times (**C3**) prior to dialysis. Since sequential centrifugation is ubiquitous in the purification of laboratory-made CNCs, the centrifuged samples (**C1**, **C2** and **C3**), which showed no significant differences between each other, will be referred to as “standard” CNCs. Additional modification of the CNC morphology was subsequently explored by applying a further post-treatment to induce partial aggregation, as illustrated in **Figure 1b**. In this step, **C0** and **C3** CNCs were centrifuged in the presence of calcium chloride followed by dialysis, to respectively produce **C0-Ca** and **C3-Ca**, also collectively referred to as Ca-CNCs.

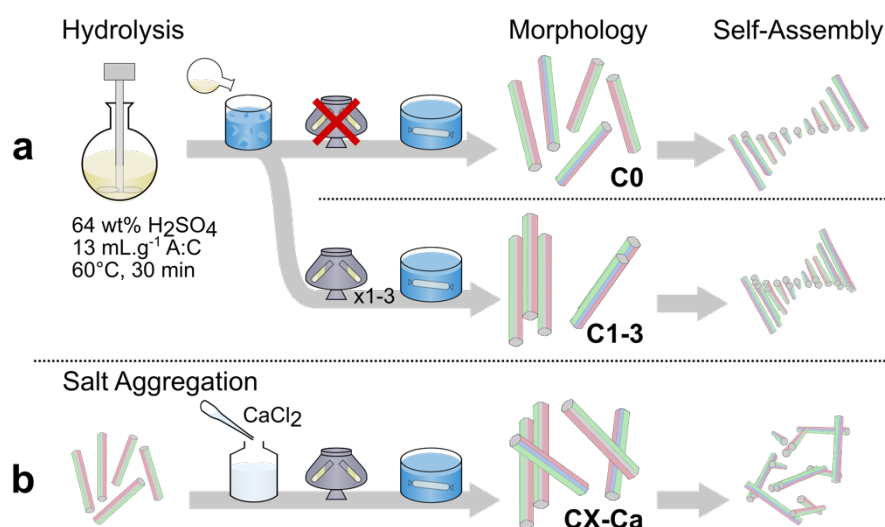


Figure 1. Scheme summarizing the preparation, purification, and resulting liquid crystalline behavior after concentration of (a) never centrifuged (**C0**), “standard” CNCs (i.e., centrifuged one to three times) (**C1-3**) and of (b) CNCs aggregated by calcium chloride addition followed by centrifugation (**C0-Ca** & **C3-Ca**).

2.2 Morphology of the CNCs

To understand whether centrifugation drives the formation of bundled particles, the size and morphology of the CNCs were imaged by TEM, as exemplified in **Figure 2a**. Visual inspection revealed that in all samples most particles exhibited bundled or aggregated morphology, as commonly reported for wood and cotton CNCs.^[5,6] To quantify their shape and dimensions, we considered each discrete object on the TEM grid as a single CNC, irrespective of whether it appeared as a single crystallite or as a composite object formed by multiple overlapping crystallites. By applying this systematic rule, CNCs were manually contoured, and their morphology descriptors were extracted (see Experimental Section for more details). The resulting dimensions from TEM, alongside the mean hydrodynamic diameter values obtained by dynamic light scattering (DLS), are reported in **Figure 2**.

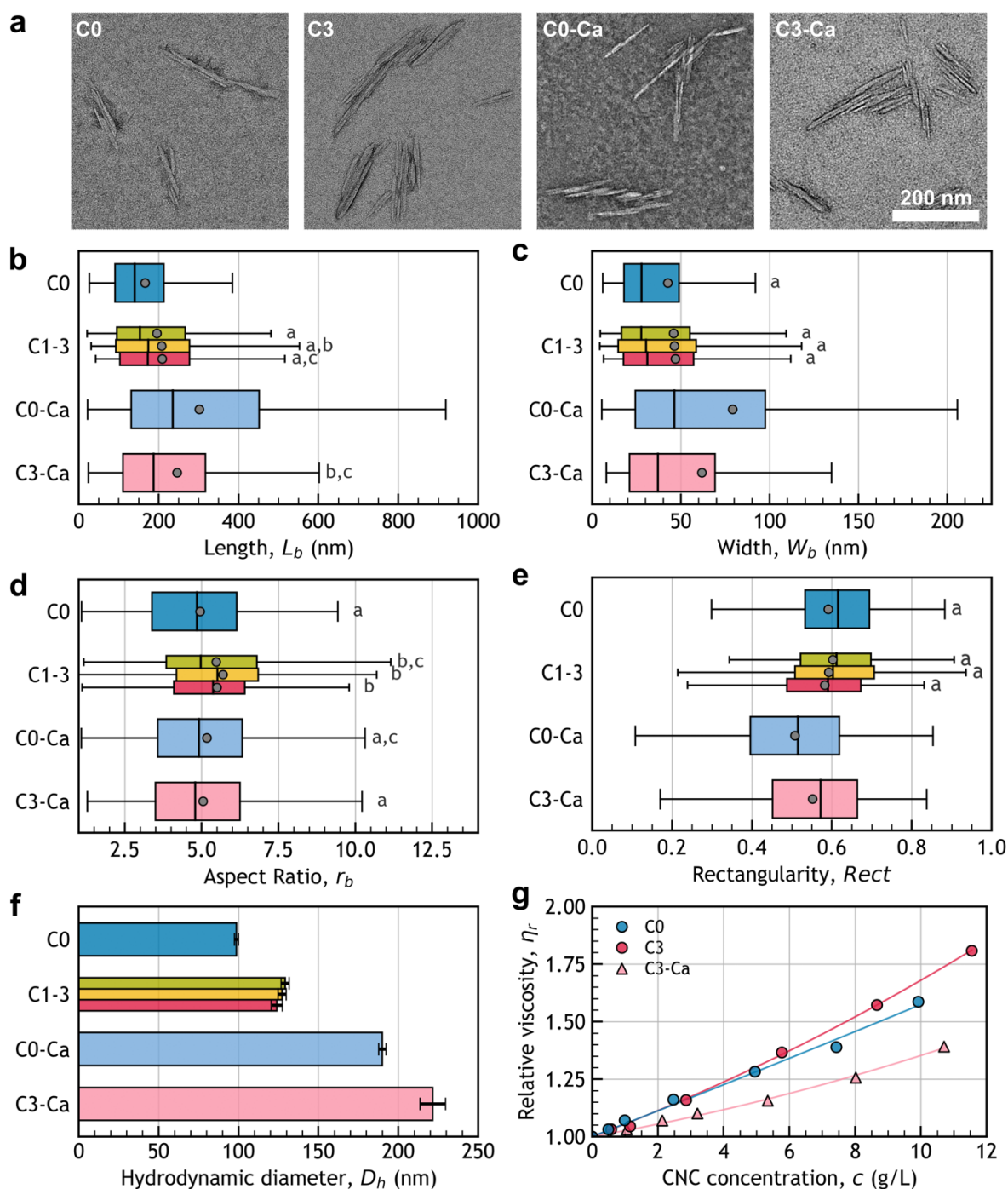


Figure 2. Analysis of the CNC morphology. (a) Typical objects observed by TEM and corresponding boxplots of the morphological parameters extracted from the TEM images: (b) bounding box lengths (L_b), (c) bounding box widths (W_b), (d) bounding box aspect ratios ($r_b = L_b / W_b$), and (e) rectangularity ($Rect = A / [L_b W_b]$, where A is the particle projected area). Outliers were not displayed; the grey round markers indicate the number average values. Sample distributions were compared using a Mann-Whitney test on the natural log of the data (L_b and W_b) or on the data directly (r_b and $Rect$), samples that share the same letter (a, b, or c) were not statistically different within a 0.05 threshold p -value. Complementary analysis through ensemble measurements in suspension by DLS, with (f) average

hydrodynamic diameter (D_h) and by viscosity, with (**g**) evolution of the relative viscosity (η_r) as a function of the CNC concentration (c) and best fit using $\eta_r = 1 + [\eta]c + k_H[\eta]^2c^2$ of **C0** (blue circles), **C3** (red circles) and **C3-Ca** (red triangle).

Size characterization indicates that standard CNCs are larger than never-centrifuged CNCs. From TEM analysis, the bounding box length (L_b) and width (W_b) of all samples followed a rather log-normal distribution (see **Figure S1 & Table S1**).^[5,10] The dimensions of standard CNCs (**C1-3**) were all similar to one another, while **C0** exhibited a smaller hydrodynamic size and significantly lower lengths. These results indicate that centrifugation leads to the formation of larger CNCs through the formation of composite particles. Interestingly, we observed that the increase of size (L_b and hydrodynamic diameter) was obtained only in the first cycle of centrifugation, with the particle size remaining constant within statistical significance upon further rounds of centrifugation.

The morphology of the particles was investigated further through estimation of the bounding box aspect ratio (r_b) and rectangularity (*Rect*) using:

$$r_b = \frac{L_b}{W_b} \quad (1)$$

and

$$Rect = \frac{A}{L_b W_b} \quad (2)$$

where A is the particle projected area. Both values followed skewed normal distributions for all samples (see **Figure S2 & Table S1**). On average, **C0** exhibited lower aspect ratios than the standard samples (**C1-3**), but all had a similar rectangularity, confirming that centrifugation led to the formation of dense self-similar composite particles. For rod-like particles, this scaling indicates that the units constituting the composite particles are aligned.

Conversely, post-treatment with calcium chloride led to irregular association into bigger particles. The TEM and DLS dimensions of **C0-Ca** and **C3-Ca** were larger than the other samples, irrespective of the initial CNC used to prepare them. This shows that exposure to calcium chloride led to particle association that was retained after extensive dialysis. The Ca-CNCs also exhibited the same aspect ratio as the never-centrifuged CNCs, but with a lower rectangularity than all other CNCs. The lower aspect ratio and rectangularity of the Ca-CNCs indicate that they are composed of misaligned components. This is consistent with extended DLVO predictions for charged elongated rods, for which a preferential crossed association offers a lower energetic barrier to overcome to allow for rapid aggregation.^[11,12] This association mechanism is favored at high ionic strength^[13] and was experimentally observed for charged CNCs.^[14-16]

To confirm that the observed morphologies were not due to imaging artefacts arising from the TEM sample preparation, the samples were also imaged by Cryo-TEM (as exemplified in **Figure S3**). These images show that **C0** and **C3** appear laterally associated with rare occurrences of crossed objects, whereas **C3-Ca** exhibits significantly more misaligned objects. While Cryo-TEM does not provide statistically representative results, these qualitative

observations are consistent with the quantitative TEM analysis presented earlier. This validates the interpretation of a genuine discrepancy of aggregation states between these particles in suspension rather than arising from TEM sample preparation.

To validate the morphological analysis of CNCs by TEM, the three-dimensional (3D) aspect ratio of the samples was estimated from viscosity measurements. Indeed, the use of TEM images to assess CNC dimensions and morphologies presents several limitations: the measurements can be influenced by the sample preparation, are based on a limited number of objects, and are sensitive to human bias upon manual segmentation.^[10,17] Alternatively, viscosity measurements can be used to estimate the average aspect ratio of CNCs through the calculation of the intrinsic viscosity.^[18] The main advantage of this complementary method over TEM analysis is that it offers an unbiased, ensemble measurement sensitive to the 3D shape of the suspended particles, while also being exempt of drying artefact, simple, accessible and quick to implement.

The prolate spheroid equivalent 3D aspect ratio $r_{3D} = L/d$, where L and d are respectively the major and minor axis respectively, can be calculated from the intrinsic viscosity, $[\eta]$ (m g^{-1}) according to:^[19,20]

$$[\eta] = \frac{8}{15} \frac{(r_{3D}^4 - 1)}{\rho_{CNC} r_{3D}^2 \left[\frac{(2r_{3D}^2 - 1) \cosh^{-1}(r_{3D})}{r_{3D}(r_{3D}^2 - 1)^{0.5}} - 1 \right]} \quad (3)$$

where ρ_{CNC} is the density of a CNC particle ($\rho_{CNC} = 1.6 \text{ g mL}^{-1}$). The intrinsic viscosity, $[\eta]$ and the unitless Huggins coefficient (k_H), which depends on objects interactions, can be obtained by fitting the Huggins equation:^[21]

$$\eta_r \approx 1 + [\eta]c + k_H[\eta]^2c^2 \quad (4)$$

where η_r is the relative viscosity and c (g mL^{-1}) is the particle concentration. Therefore, fitting of the relative viscosity as a function of the particle concentration allows for the determination of the intrinsic viscosity, from which the 3D aspect ratio can be extracted.

The viscosity measurements indicates that Ca-CNCs present a smaller 3D aspect ratio than both the never-centrifuged CNCs and the standard CNCs. The evolution of the relative viscosity as a function of the particle concentration presented in **Figure 2g** was used to extract the intrinsic viscosity and the 3D aspect ratio presented in **Table S3**. Samples **C3** and **C0** exhibited similar behavior, with close intrinsic viscosities (54 and 56 mL g^{-1} respectively) and Huggins coefficients (0.5 and 0.1 respectively), resulting in a 3D aspect ratio of 35 for both **C3** and **C0**. Compared to **C3** and **C0**, **C3-Ca** presented a smaller intrinsic viscosity (25 mL g^{-1}) and a higher Huggins coefficient (1.6). It resulted in a lower 3D aspect ratio of 22, showing that Ca-CNCs are less elongated than **C0** and **C3**. The Huggins coefficients are in the range previously reported for CNCs and other comparable charged elongated nanoparticles.^[22,23] The higher value for **C3-Ca** suggests that it displays stronger inter-particle interactions (either repulsive or attractive).

The 3D aspect ratios estimated above from viscosimetry are considerably higher than the ones typically estimated from the TEM or AFM particle analysis.^[18,24–26] Such analysis often considers a circular CNC cross-section, yet CNCs usually have anisotropic cross-sections, with thicknesses often two to three times smaller than their widths.^[6] This causes the CNCs to lay

flat on the substrate, and systematically present their thicker dimension in a top-view, 2D morphological analysis, which biases the apparent aspect ratio to lower values. However, the apparent aspect ratio obtained from viscosity measurements can also present some biases. Using this technique for charged particles can lead to an overestimation of the apparent aspect ratio due to the electroviscous effects.^[18,27] Nevertheless, comparison between the samples gives valuable insight into their relative morphology. Consequently, the viscosity measurements confirmed the similarity of shape between never-centrifuged and standard CNCs while highlighting the lower aspect ratio of the Ca-CNCs, in accordance with the TEM and Cryo-TEM observations.

2.3 Local Orientation of Crystallites in the CNCs

The relative arrangement of crystallites in the composite particles might result from preferential crystal plane interactions. In cotton fiber, native crystallites occur mainly in the cellulose I β crystalline allomorph and are believed to possess irregular hexagonal-like cross-sections as illustrated in **Figure 3a**.^[28] Consequently, the vast majority (approx. 80%) of the exposed crystal surfaces corresponds to the (110) and (1-10) planes, with the remaining surfaces corresponding to the (100) plane. The presence of various exposed surfaces can lead to different relative orientations and interacting surfaces among the individual crystallites constituting the composite particles. The greater density of hydroxyl groups on the (110) and (1-10) planes is expected to make these faces more hydrophilic than the (100) plane, which is sometimes described as “hydrophobic” by comparison. Consequently, the distribution of exposed crystal surfaces on the crystallites is likely to influence their relative orientation upon mutual association, with implications for CNC surface chemistry and their interactions.

The nanoscale structure of the particles was investigated by scanning nanobeam electron diffraction (SNBED). This technique allows for the mapping of the local crystal orientation of crystallites in the CNCs by scanning them with a focused electron probe and collecting 2D electron diffraction (ED) patterns at each scanning position, as illustrated in **Figure 3b**. Each ED pattern was collected by an electron probe with a diameter of 25 nm, so the diffraction information combines all crystallites within the probe diameter. Each scan position containing an ED pattern (considered a “pixel”) was indexed according to the cellulose I β unit cell. This information was used to deduce the local crystal orientation parallel to the electron beam (and therefore perpendicular to the TEM grid) and subjected to the statistical analysis shown in **Figure 3c** and **3d**. Examples of SNBED data are illustrated in **Figure S5**.

The analysis of the SNBED data revealed, as evidenced by the ratio between the different observed crystal orientations presented in **Figure 3c**, that crystallites are not randomly oriented on the TEM grid. For the never-centrifuged CNCs (**C0**), 44% of the measured crystallite area corresponded to the [010] zone-axis, with the remaining 56% divided between the [110] and [1-10] zone axes. In contrast, for the standard CNCs (**C3**) and the Ca-CNCs (**C0-Ca** and **C3-Ca**), the [010] zone-axis was found for a considerable majority of the measured pixels (79%, 82%, and 74% respectively). For all samples, none of the measured diffraction patterns corresponded to the [100] zone axis, indicating that the crystallites never lay with their hydrophobic faces touching the grid. This absence is likely due to the poor adhesion between the hydrophobic (100) surface and the hydrophilic glow-discharged carbon film of the TEM grid.

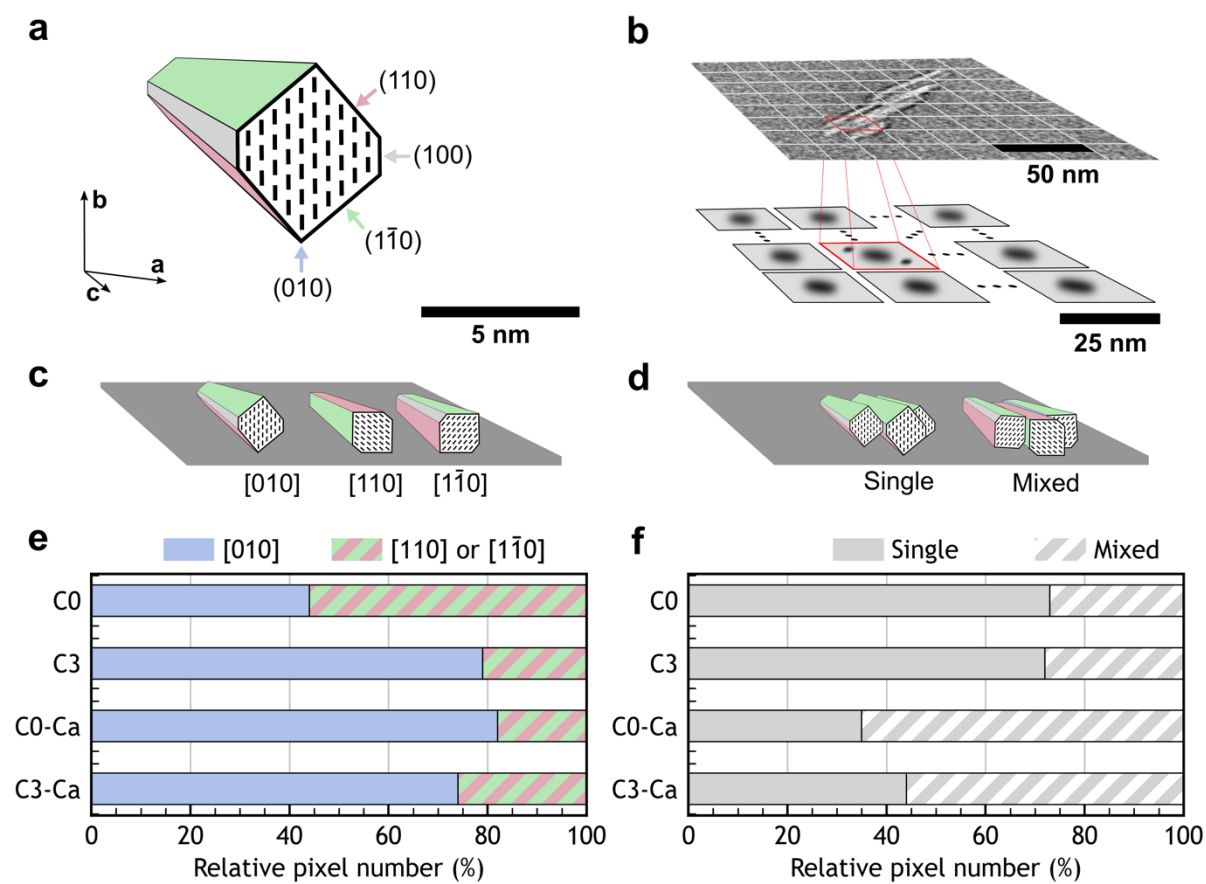


Figure 3. Local orientation of the crystallites constituting the cellulose nanocrystals probed by scanning nanobeam electron diffraction (SNBED). **(a)** Cross-section of native cellulose crystal from cotton ($I\beta$) and corresponding crystallographic planes. **(b)** Illustration of the diffraction pattern mapping by SNBED. **(c)** Corresponding relative pixel number per cellulose crystal plane direction and **(d)** relative number of pixels belonging to discrete particles exhibiting one crystal orientation (Single) compared to a mix of crystal orientations (Mixed).

The prevalence of the $[010]$ zone axis for all samples in **Figure 3c** is unexpected from a geometrical point of view, which could be explained by two non-exclusive hypotheses. Assuming the conventional hexagonal-like cross-section expected for a cotton cellulose crystal, this orientation would correspond to the crystallite standing awkwardly on the sharp edge at the intersection of the $(1-10)$ and (110) planes (**Figure 3a**). Such a configuration is highly unlikely both for individual crystallites and for randomly associated composite particles. In the case of individual crystallites, the prevalence of $[010]$ zone axis may indicate a change in the cross-sectional shape during the hydrolysis through the etching of the crystal edge, exposing the (010) faces. A similar etching has previously been observed for tunicate CNCs,^[29] and has been suggested in multiple previous studies.^[30–32] In the case of composite particles, the prevalence of the $[010]$ zone axis indicates that crystallite association is not occurring at random mutual orientations. If crystallites could associate equally along all their crystal faces and there was no

preferential interaction between the crystals and the grid, the relative proportion of crystal orientations would be equiprobable. If the observed prevalence of the [010] zone axis was only due to a preferential interaction between the crystal and the grid, the formation of bigger composite particles would lead to a similar or lower proportion of the [010] zone axis. However, the opposite trend is observed, indicating that composite particles are not formed of randomly attached crystallites, but rather preferentially associated through their (100) crystal faces. The ability of CNC crystallites to organize into similar structures has been hypothesized previously.^[30,31,33]

Further analysis of the ED data confirms that bundle-like CNCs are made of preferentially oriented crystallites. The ED data was used to classify the CNCs based on the number of observed crystal orientations within individual particles: “Single” particles were composed of crystalline regions oriented along a single crystallographic axis, while “Mixed” particles contained crystalline regions oriented along different crystallographic axes. The relative occurrence of each particle type (as a proportion of the total pixels) is shown in **Figure 3d**. For the never-centrifuged (**C0**) and the standard (**C3**) samples over two-thirds of the pixels corresponded to Single particles (73% and 72% respectively). In contrast, much fewer Single particles were observed for the Ca-CNCs (**C0-Ca** Single and **C3-Ca** Single particles corresponded to 35% and 44% of the pixels, respectively).

The observed prevalence of [010] zone axis for all samples, combined with the prevalence of Single CNCs in **C0** and **C3** samples, strongly support that the bundle-like particles formed during centrifugation result from the association of crystallites through their hydrophobic faces (100). The sample **C3** exhibited a high proportion of particles made up of crystallites with a single orientation (**Figure 3d**). This implies that for both samples the association between individual crystallites is uniform within single particles and occurs through identical surfaces. The high ratio of [010] orientations observed in **C3** indicates that the individual crystallites are associated predominantly through (100) surfaces (**Figure 3c**), resulting in a highly anisotropic cross-sectional shape elongated perpendicular to the [010] direction. Overall, these results suggest that composite particles in the standard CNCs are raft-like composite particles made from crystallites preferentially associated through their hydrophobic (100) faces.

The comparison of [010] zone axis prevalence and Single/Mixed prevalence between never-centrifuged and standard CNCs is also consistent with a smaller proportion of these hydrophobically-stabilized raft-like CNCs in never-centrifuged CNCs. Indeed, the **C0** and **C3** samples both showed a high degree of Single orientations, yet with a lower degree of preferential orientation for **C0** along [010] (**Figure 3c** and **3d**). These observations are expected if never-centrifuged composite particles of more isometric cross-section can rotate more freely about their long axis when landing on the grid surface, while standard CNCs containing more raft-like particles of anisometric cross-section can only lie flat onto the grid and thus select the [010] zone axis orientation.

In contrast, the analysis of Ca-CNCs with SNBED leads to very different observations, which is indicative of a random aggregation mechanism. Considering the calcium-induced aggregation of standard CNCs, we see that **C3-Ca** contains mainly particles with mixed crystal orientations while retaining the overall prevalence of crystallites laying along [010] (**Figure 3c** and **3d**). The high proportion of mixed crystal orientations in **C3-Ca** indicates that the

composite particles formed through calcium-induced aggregation were occurring at more random mutual orientations, unlike for **C3**. However, due to the presence of pre-existing raft-like particles in **C3** that aggregated further but less selectively in **C3-Ca**, the overall prevalence of [010] orientation of **C3** was partially retained. In this regard, it is interesting to consider the case of calcium-induced aggregation of never-centrifuged CNCs, as this sample forms from particles with a smaller degree of alignment prior to the onset of aggregation and can be expected to yield a lower degree of alignment. Surprisingly, **C0-Ca** exhibited a similar trend to **C3-Ca**, namely, it displayed a high proportion of [010] orientations that is similar to all the other samples containing a high number of big raft-like particles. This suggests that the directionality of the hydrophobic interactions along the [100] direction still plays a role in aggregating samples until they are no longer as available as they were in a sample of low aggregation state (e.g. in the **C0** sample).

2.4 Suspension and Surface Properties

The liquid crystalline properties of the different CNCs can be investigated through the evolution of the volume fraction of anisotropic phase (ϕ_{ani}) and cholesteric pitch as a function of the CNC concentration, here reported in weight fraction (w_{CNC}). The ϕ_{ani} usually appears above a first threshold weight fraction of CNC and increases with w_{CNC} until all the suspension is fully cholesteric above a second threshold concentration. According to the Onsager model for achiral hard rods, these threshold concentrations scale inversely proportional to the aspect ratio of the rods, and thus are informative of the change in average CNC aspect ratio. Experimentally, ϕ_{ani} can be estimated as the fraction of bright sample to total sample volume from the observation of capillaries between crossed polarizers. However, if the samples are kinetically arrested, they can also macroscopically shear-align during the capillary filling and remain trapped with this alignment, resulting in a nearly 100% ϕ_{ani} . A steep increase of ϕ_{ani} with increasing CNC weight fraction can thus also be indicative of early gelation. Complementary to measuring ϕ_{ani} , the cholesteric pitch p usually decreases as the CNC weight fraction increases,^[34,35] and its inverse $1/p$ can be used as a measure of the chiral strength of the interactions between neighboring CNCs. This estimation is however effective only if the suspension is capable of relaxing towards a cholesteric state after the shear experienced upon filling the capillary and relies on the sample not being arrested.

The investigation of the liquid crystalline properties indicates that **C3** exhibits stronger chiral interactions than **C0**. The phase diagrams in **Figure 4a** reveal a narrower biphasic regime for **C3** shifted to lower concentrations, indicative of CNCs of higher aspect ratios. The corresponding evolution of the pitch as a function of the CNC weight fraction in **Figure 4b** reveals that **C3** has a smaller pitch than **C0**, which also indicates that the standard CNCs had stronger chiral interactions. These observations are in accordance with the positive correlation between chiral strength and bundle content that we reported previously.^[6] These results suggest that the additional centrifugation step leading to **C3**, and commonly applied during the laboratory production of standard CNCs, is responsible for the formation of additional chiral bundles of increased chiral strength.

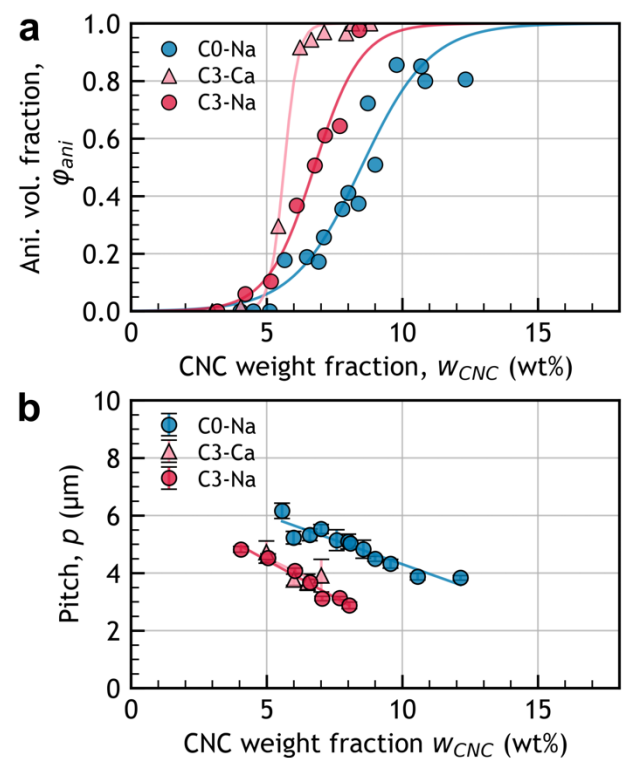


Figure 4. Liquid crystalline properties of different CNC suspensions with (a) anisotropic volume fraction (ϕ_{ani}) and (b) pitch (p) as a function of CNC weight fraction (w_{CNC}) for **C0** (blue circles), **C3** (red circles) and **C3-Ca** (red triangles). Fitting lines are shown as a guide.

The comparison of **C3-Ca** with **C0** and **C3** reveals further trends that can be associated with early gelation and interrupted phase transition into a cholesteric. Indeed, the interpretation of the evolution of the reported anisotropic volume fraction and pitch for **C3-Ca** is less straightforward as they exhibited distinctive shear-alignment under crossed polarizers (**Figure S6**), indicating that the sample was kinetically arrested and was not able to relax over time. Such gelation at a low CNC volume fraction can be caused by the greater hydrodynamic volume induced by the misaligned composite particles. Despite these clear signs of gelation, **C3-Ca** exhibited some fingerprint patterns arising from isolated tactoids. The evolution of the pitch of these tactoids as a function of the CNC weight fraction followed the same trend as for **C3**. This suggests that some of the starting **C3** CNCs remained unchanged upon calcium-induced aggregation, retaining their ability to form a cholesteric phase in **C3-Ca**. Overall, these observations agree with the presence of misaligned composite particles in **C3-Ca** compared to **C3**, compromising the colloidal stability of **C3-Ca** by promoting early gelation without modifying the chiral strength.

Altering the surface properties of CNC can have important consequences on their liquid crystalline properties and thus the charge of the different samples was characterized through titration, elemental analysis and ζ -potential measurements to identify possible changes (**Table S4**). Conductometric titration against sodium hydroxide revealed that standard (**C3**) and never-centrifuged CNCs (**C0**) exhibited comparable surface charge per mass. Zetametry revealed a comparable ζ -potential around -50 mV, ascribed to the grafting of sulfate-half ester groups

during the hydrolysis, and providing the required colloidal stability. The similarity in the surface properties suggests that the differences in liquid crystalline properties were not dictated by a change of surface chemistry, but solely by a change of morphology. Moreover, their comparable specific charge per mass, despite the obtention of larger objects, indicates that all surface charges initially present in **C0** were still available in **C3**. This indicates that the surface sulfate half-ester groups were not hidden in between crystallites upon their association.

Comparison of Ca-CNCs with **C0** and **C3** reveals a clear decrease of surface potential for Ca-CNCs, with a ζ -potential around -35 mV (vs -50 mV for **C1-3**, **Table S4**). To measure the structural charge of Ca-CNCs, conductometric titration against sodium hydroxide is not relevant since it only measures the amount of present H^+ ions, the latter being equal to the amount of negative $-OSO_3^-$ grafted groups only in the absence of any other cation. Instead, we estimated the amount of Ca^{2+} ions in **C3-Ca** using elemental analysis, which yielded a calcium content of 133 mmol kg^{-1} , corresponding to half of the surface charges measured for its 'parent' **C3** sample, i.e., before the introduction of Ca^{2+} ions in that sample. Given the divalent character of Ca^{2+} , this indicates that all the charges on the **C3-Ca** were in the form of calcium salt and that they were not hidden during the aggregation process. This charge coverage with Ca^{2+} could be the main reason for the lower colloidal stability of Ca-CNCs, its lower absolute ζ -potential and its higher Huggins coefficient compared to **C0** and **C3**. This reduction of colloidal stability could be attributed to the screening of the surface charges by the metallic cations adsorbed onto the surface.

Given that the investigated post-treatment methods result in particles with fundamentally different composite morphologies, it is interesting to also assess whether their relative mechanical cohesion is different. For this, the evolution of their hydrodynamic diameter was monitored with increasing ultrasonication (**Figure 5a**). For all samples, the rate of size reduction decreased with increasing ultrasonication dose. Specifically, the hydrodynamic diameter exhibited a stretched exponential decay as a function of the added sonication energy, before reaching a plateau of $59 \pm 2 \text{ nm}$ for sonication doses greater than 445 J mL^{-1} . Modeling of the evolution of the size with the sonication dose with a simple dissociation function overlooked certain features at intermediate sonication dose (see **Figure S7**, **Table S5**, and the corresponding discussion in the Supporting Information). Instead, the curves were modeled by the modified dissociation rate functions shown in **Equations 7** and **8**, whose best fitting parameters are presented in **Table S6**. The best-fitting parameters for **C0** and **C3** were used to extract the specific rate of size reduction of the particles formed by calcium-induced aggregation using **Equation 8**. This expression assumes that the size reduction for calcium-induced composite particles is independent and simultaneous to the size reduction for the bundle particles. The size evolution was then used to extract the sonication-dependent rate constant of size decrease (k'), expressed in **Equation 6**, and to plot the rate of size decrease ($k'D$) in **Figure 5b**.

C3 and **C0** exhibited similarly decaying rates that were lower than the rates of **C3-Ca** and **C0-Ca** for any given ultrasonication dose. The higher rates of size decrease for calcium-aggregated particles indicate that they were less cohesive. This results from the higher energetic configuration predicted for crossed-associated CNCs compared to laterally associated CNCs.^[11] Importantly, the loss of size exhibited by **C3-Ca** and **C0-Ca** is likely amplified by the change of shape induced by the breaking of the misaligned composite particles. Indeed, DLS measures the apparent hydrodynamic diameter of the particles, therefore the breaking of an irregular object leads to a bigger apparent size decrease than the breaking of a laterally associated one.

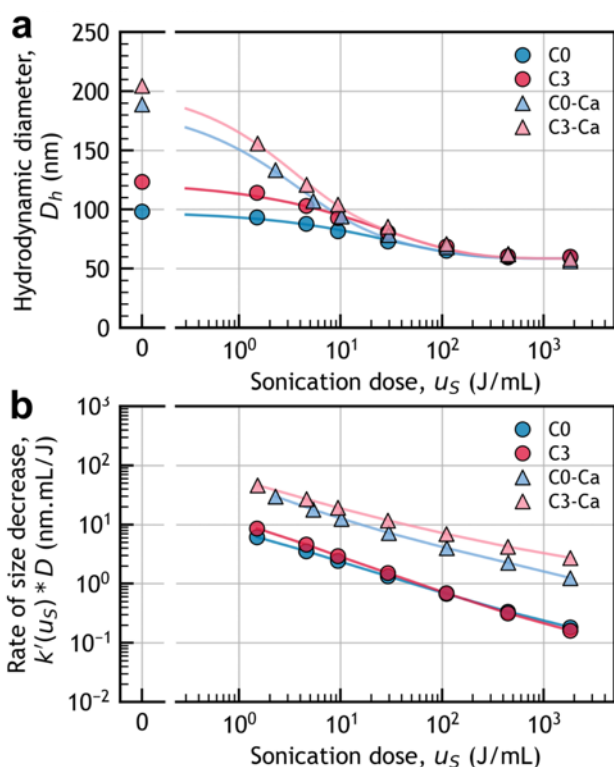


Figure 5. Impact of ultrasonication dose (u_s) on (a) the hydrodynamic diameter and on (b) the corresponding rate of size decrease ($D k'(u_s)$). The evolution of the hydrodynamic diameter was fitted using **Equations 7 & 8** and the corresponding dose-dependent rate was calculated from the best fit using **Equation 5 & 6**. With **C0** (blue circles), **C3** (red circles), **C0-Ca** (blue triangles), and **C3-Ca** (red triangles).

2.5 Investigation of the Salt-Induced Aggregation

Since calcium-induced aggregation leads to the formation of randomly associated composite particles retained after dialysis, it suggests that this effect depends on the preparation conditions and that it can be exploited to control the size of the final particles. Therefore, following the protocol presented in **Figure 6a**, the impact of salt-induced aggregation on the properties of the CNC suspension and on their hydrodynamic diameter after redispersion and dilution in deionized water were investigated over a range of conditions. We explored the impact of the salt cation (NaCl vs CaCl_2) and ionic strength (0 to 80 mM) at fixed CNC weight fraction (~6.50 wt%) on the properties of the suspension in two steps: first, after salt addition and centrifugation, where a gel may form, and second, after redispersion and dilution to a stable, 0.1 wt% CNCs, suspension having an ionic strength as close as possible to 1 mM.

In the gel formation step, the obtained aggregated CNC suspension was qualitatively inspected. Increasing the ionic strength led overall to stronger gels over the range of ionic strengths studied. For both salts, increasing the ionic strength from 0 to 80 mM led to the formation of gels exhibiting a greater cohesion that required an increasing effort to be redispersed, as expected from an increase in gel strength. Above 30 mM of ionic strength, centrifugation led to biphasic

systems made up of a bottom birefringent arrested phase, and an upper clear liquid layer. The density of the arrested phase increased with increasing ionic strength, as visually indicated by its lower volume.

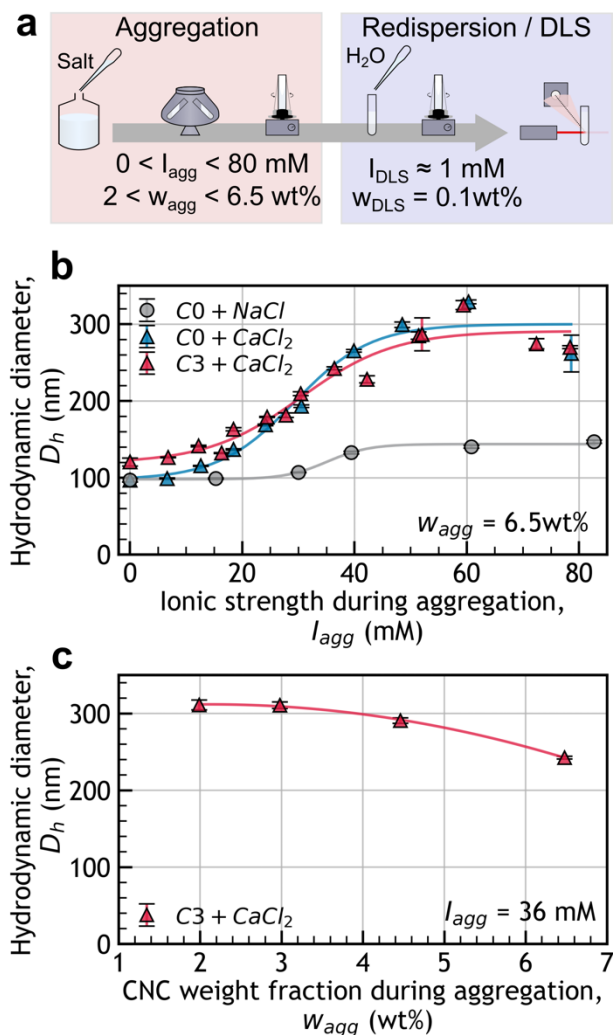


Figure 6. (a) Scheme of the calcium aggregation process and the resulting impact of (b) salt type and ionic strength (I_{agg}) or (c) CNC mass fraction (w_{agg}) during aggregation, on the hydrodynamic diameter (D_h) of samples **C0** and **C3**. The lines of best fit, presented as visual guides, were obtained from (b) a sigmoid or (c) a second order polynomial.

In the second step, the obtained CNC suspensions were redispersed, diluted and their hydrodynamic diameter was measured. The time between sample centrifugation and their dilution for measurement varied from 0 to 63 days without significant impact on the hydrodynamic diameter trend, as presented in **Figure S8**. The evolution of the hydrodynamic diameter was highly dependent on the salt type and ionic strength, as illustrated in **Figure 6b**. When sodium chloride was used to increase the ionic strength of never-centrifuged CNCs (**C0+NaCl**), the suspension redispersed easily and a moderate size increase from ~ 100 nm was

observed only above 30 mM and quickly reached a plateau of ~ 145 nm above 50 mM. In contrast, when calcium chloride was used to increase the ionic strength, a much stronger evolution of the size was observed for both never centrifuged and classical CNCs (**C0**+**CaCl₂** and **C3**+**CaCl₂**). The hydrodynamic diameter followed a sigmoidal evolution, starting to increase from ~ 100 - 120 nm at an ionic strength of 12 mM before reaching a plateau around 290 nm above 50 mM. Finally, increasing the ionic strength above 40 mM led to greater variability of the sample sizes around the overall trend (290 ± 25 nm), and macroscopic inhomogeneities could be seen by naked eye above 50 mM.

These results suggest that divalent ions are more potent than monovalent ions for inducing aggregation of CNCs, as previously demonstrated for different polycations.^[9,16,36,37] This can be explained by the formation of calcium bridges between CNCs, in addition to any shielding of the electrostatic interactions. Consequently, gels made from calcium chloride seemed denser and stronger, as previously observed by other studies.^[37,38] This calcium bridging also explains the irreversibility and magnitude of the particle size increase upon the addition of calcium ions as opposed to the moderate size increase observed upon the addition of sodium ions.

The stable and moderate size reached after the addition of sodium chloride above a concentration threshold might be explained by the formation of bundles. Indeed, the SNBED measurements of **C0**-**Ca** suggest that a high ionic strength leads to bundle formation. Plus, previous work showed that NaCl-induced aggregation of standard CNCs was reversible upon dialysis.^[39] In our conditions, sample dilution leads to a dramatic reduction of the salt concentration, effectively mimicking the impact of dialysis on a CNC suspension. Consequently, we would expect the **C0**+**NaCl** aggregates to be broken down into the starting CNC upon dilution, which should lead to a constant hydrodynamic size. Instead, the hydrodynamic diameter increased slightly and then reached a plateau at a size similar to **C3**, which could be indicative of an irreversible formation of bundles. This hypothesis should be checked by comparing never-centrifuged and centrifuged CNCs aggregated with NaCl and then dialyzed.

For a given ionic strength at which the gelation was triggered (36 mM of calcium chloride), the CNC weight fraction at which the aggregation was triggered was found to influence the final particle size after dilution of the gel, with higher weight fractions leading to smaller hydrodynamic sizes (**Figure 6c**). Indeed, lowering the CNC mass fraction from 6.5 to 2.0 wt% led to an increase of the particle size after aggregation from 243 to 311 nm. To our knowledge, no study reported the impact of CNC mass fraction on the particle size change after calcium chloride aggregation followed by dilution. A previous study showed that lowering the CNC mass fraction from 6 to 2 wt% in the presence of calcium chloride leads to a decrease of the viscosity.^[38] This indicates that particles move more freely at low CNC mass fraction, making the formation of new stable composite particles more likely.

Finally, aggregation time (up to ~ 8 days) and centrifugation conditions (0, 1 or 2 centrifugation cycles) have been varied at fixed calcium chloride concentration (51.4 mM) and CNC weight fraction (**C3** at 6.49 wt%) and the resulting hydrodynamic diameter of the redispersed and diluted samples are presented in **Table S7**. In these conditions, the waiting time before redispersion and dilution seemed to have a negligible impact after 1 h. Applying any number

of centrifugation cycles led to similar sizes, indicating that the number of centrifugation cycles did not influence the size of the particles after dilution.

3. Conclusions

CNC morphology and size were tuned by modifying the post-hydrolysis purification protocol. Specifically, the centrifugation step applied in most CNC extraction protocols at the laboratory scale was shown to be responsible for the formation of additional CNC “bundles” with raft-like morphology, that displayed enhanced chiral strength. These raft-like particles resulted from the preferential lateral association of crystallites through their hydrophobic faces, which occurs without screening the surface half-ester charges. Consequently, the resulting CNCs exhibit a lower proportion of hydrophobic surfaces, which is expected to influence their surface properties, and notably their amphiphilicity.^[40]

Aggregation of purified CNCs by exposure to by calcium chloride at high ionic strength was also used to irreversibly increase the particle size in a controllable fashion. After dialysis, the obtained CNCs were in the form of calcium salts and exhibited a clear increase of the proportion of composite particles with a misaligned morphology. Due to their high hydrodynamic volume, these crossed objects exhibited enhanced gelation, which could be of interest in some applications.

While these findings are only based on the analysis of CNCs obtained from sulfuric acid hydrolysis of cotton, CNCs extracted from wood and/or obtained by other production methods also typically display a dominant proportion of bundled particles, suggesting that these trends could be valid across all these systems and prompting further investigations in this direction. This is especially important to consider for the use of commercial CNCs, which, unlike laboratory-made CNCs, often undergo ultrafiltration instead of centrifugation in their purification processes,^[41] and thus impact their particle morphology and their chiral properties. This work, despite fundamental, pinpoints previously unexplored possibilities with immediate practical manufacturing considerations for commercial applications of CNCs where their chiral liquid crystalline properties are directly exploited (e.g. cellulose-based glitter), but potentially in any other situation where the CNC aggregation state is key.

4. Experimental Section

Materials: Sulfuric acid (H_2SO_4 , $\geq 95\%$, analytical grade), sodium hydroxide (NaOH, 99%, pellets), sodium chloride (NaCl, $\geq 99.5\%$, laboratory grade, calcium chloride (CaCl_2 , fused granular) and hydrogen peroxide (H_2O_2 , > 30 w/v%, laboratory reagent grade) were provided by Fisher Scientifics. All the water used was MilliQ grade (Millipore, Synergy UV system).

Data processing was performed with custom-made Python script. Statistical analysis and fittings were performed with the Scipy library. The presented error on the fitting parameters corresponds to their standard deviation error calculated from the covariance matrix (pcov).

CNCs suspensions were produced by sulfuric acid hydrolysis of cotton-based filter paper (Whatman No. 1). Shredded filter paper (15 g, CookWork coffee grinder) was introduced to 300 g of a 64 wt% sulfuric acid solution ($\rho = 1.543 \text{ g mL}^{-1}$) preheated to 60 °C. After 30 min

of hydrolysis under vigorous mechanical stirring, the medium was quenched with 300 mL of ice-cold water. Part of the mixture was centrifuged (20,000 g, 20 min, 4 °C, Lynx 6000 Thermo Scientific) and the resulting pellet redispersed in water. This process was repeated to produce aliquots of CNCs that had never been centrifuged (**C0**), centrifuged once (**C1**), twice (**C2**), and three times (**C3**). All samples were dialyzed against MilliQ water (MWCO 12-14 kDa, Medicell membrane), with the water changed at least once a day until the conductivity was stable (~2 weeks).

CNC mass fraction was obtained from gravimetric analysis by drying the suspensions in an oven (65 °C, > 40 h). The mass of dry CNC was at least 15 mg and measurements were made in triplicate.

CNC surface charge was obtained from conductometric titration of CNC suspensions diluted in water (\approx 180 mL) in the presence of NaCl (0.2 mmol). An automatic titrator (Metrohm, 800 Dosino) was used to inject NaOH solution (10 mM Titripur®, 50 μ L min⁻¹) while monitoring the conductivity (856 conductivity module). The CNC surface charge was deduced from the first equivalence point.

Concentrated suspensions were prepared by neutralizing the suspensions with 1 molar equiv. Of NaOH per effective CNC charge followed by concentrating with a rotavapor (35°C, 20 mbar), Ca-CNC samples were further concentrated by evaporation under ambient conditions and at room temperature.

Calcium aggregated CNCs (CX-Ca) were obtained from concentrated suspensions by preparing 6.5 wt% CNC suspensions containing 13.2 ± 0.2 mM of CaCl₂, followed by a process of centrifugation (10,000 g, 20 min), redispersion (to \sim 1 wt% CNCs), and dialysis against water (\geq 2 weeks).

Salt-induced aggregates (CX+NaCl and CX+CaCl₂) were prepared by diluting concentrated CNC suspension in water before pipetting CaCl₂ or NaCl aqueous solution to form a 2 to 6.5 wt% CNC suspension in an ionic strength of 0 to 80 mM. The mixture was centrifuged (10,000 g, 20 min, Minispin Eppendorf), redispersed, then diluted for Zetasizer Measurements measurement as described below.

Calcium content was measured by inductively coupled plasma-optical emission spectrometry (ICP-OES, Thermo Fisher Scientific iCAP 7400 Duo ICP Spectrometer). Freeze-dried CNCs (\sim 20 mg) were further dried overnight in an oven (60 °C). The precisely weighed CNCs were digested for 1 h in freshly prepared piranha solution (3:1 v/v H₂SO₄:H₂O₂). A known amount of the mixture was diluted in water to obtain a solution of known concentration (\sim 3.6 wt% acid, \sim 2 g L⁻¹ CNCs) that was used for the measurement. ICP Standard (Sigma-Aldrich) were diluted with \sim 2% nitric acid (TraceMetal™ Grade, Fisher) in water (TraceSelect™ for Trace Analysis, Honeywell Riedel-de Haen™) to make the standard curve. Analysis performed on Qtegra software.

Zetasizer Measurements were performed on dilute CNC suspensions (0.1 wt%), NaCl was used to set the ionic strength as close to 1 mM as possible. Average hydrodynamic diameters were estimated in backscattering geometry (173°, 633 nm, Malvern Zetasizer Nano ZS) from three runs of 10 measurements after an initial waiting time of 5 min for the temperature to equilibrate (20– 22 °C). Zeta potentials were acquired after the hydrodynamic diameter,

through three runs of 10 measurements, analyzed using the Smoluchowski equation. Data are presented as mean \pm standard deviation.

Standard TEM observations were performed with a Talos F200X G2 microscope (FEI, 200 kV, CCD camera). A drop of CNC suspension (0.002 wt%, in 1 mM NaCl) was deposited on a glow-discharged carbon-coated copper grid. After 2 min, the excess solution was blotted with filter paper. Then, a drop of uranyl acetate aqueous solution (2 wt%) was deposited and let to set for 1.5 min before being blotted again. Particles ($N \geq 225$) were manually outlined using Fiji (ImageJ), with all touching objects considered as a discrete CNC particle. Outlines were processed using the Shape Filter plugin to extract the bounding box length (L_b), width (W_b), and the particle area (A).^[42] The bounding box aspect ratio (r_b) and rectangularity ($Rect$) were calculated from **Equations 1** and **2** respectively. Values were compared using a Mann-Whitney U test, for more details see the Supporting Information.

Cryo-TEM was performed using a JEOL JEM 2100Plus (Jeol, Japan), operated at 200 kV, equipped with a Gatan RIO 16 camera (Gatan Inc., U.S.A.). Cryo-frozen samples were prepared using an EM GP2 Automatic Plunge Freezer (Leica microsystem, Germany).

SNBED data were acquired using a JEOL 2100F operating at 200 kV equipped with a NanoMEGAS ASTAR system. The nanobeam configuration consisted of a converged electron probe of 25 nm. An ED pattern was recorded at every probe position using a Cheetah Medipix3 direct electron detector (manufactured by Amsterdam Scientific Instruments) with a 0.5 ms exposure time per probe position. The diffraction data sets were analyzed using ASTAR® facilities that are (i) crystal orientation identification through correlation with templates (i.e.: pre-computed theoretical patterns) and (ii) Virtual–Bright (VBF) and Virtual–Dark field (VDF) images reconstruction that consist in plotting the intensity fluctuations of the transmitted beam (resp. a user-selected diffracted beam) over the scanned area.

Ultrasonication of dilute CNC solutions (30 to 40 mL, 0.1 wt% CNCs, 1 mM NaCl) was performed in an ice bath using a Fisherbrand Ultrasonic disintegrator (20 kHz, $\emptyset = 12.7$ mm, pulses 2:1 sec On:Off, 40% amplitude). Samples were ultrasonicated for regular intervals of increasing time in between which aliquots were removed for analysis (1.5 mL). The dose received by each sample ($J mL^{-1}$) was calculated for each step from ultrasonication time divided by the volume of the sample and multiplied by the true power delivered (20 W, measured by Parton *et al.*^[6]). The evolution of the hydrodynamic diameter (D , nm) as a function of the ultrasonication dose (u_s , $J mL^{-1}$) was considered as a modified dissociation equation, according to:

$$\frac{dD}{du_s} = -k'(u_s) * D \quad (5)$$

with:

$$k'(u_s) = k^\alpha \alpha [u_s]^{\alpha-1} \quad (6)$$

where k' ($mL J^{-1}$) is the dose-dependent rate of size decrease, and k and α are a rate coefficient and a stretching exponent. Integrating this expression leads to:

$$D(u_s) = [D(0) - D_\infty] * \exp(-[k * u_s]^\alpha) + D_\infty \quad (7)$$

where $D(0)$ and D_∞ are the hydrodynamic diameters before ultrasonication and at infinite dose respectively. To isolate the destruction rate of aggregated CNC samples, the expression of their hydrodynamic diameter (D^{Ca} , nm) included the starting CNC used to make them, according to:

$$D^{\text{Ca}}(u_S) = [D^{\text{Ca}}(0) - D(0)] * \exp(-[k * u_S]^\alpha) + D(u_S) \quad (8)$$

For all samples, D_∞ was taken as the average of all hydrodynamic diameter at $u_S = 1827 \text{ J mL}^{-1}$, yielding $D_\infty = 59 \text{ nm}$.

Liquid crystalline properties were investigated by observations of CNC suspensions in glass capillaries. The capillaries (CM Scientific, ID = $0.3 \times 6.0 \text{ mm}^2$) were filled with a series of suspension dilutions before sealing them with nail varnish and marking the initial meniscus position (so that any evaporation could be accounted for). The anisotropic volume fraction and corrected concentration were measured from the analysis of images taken after two weeks and again after at least a further week to confirm that no further evolution occurred. The pitch was measured after two weeks using polarized optical microscopy (POM) at three different locations and with at least four different images recorded for each location ($N \geq 12$).

Relative viscosity was calculated from flow time measurements at low particle concentration by using:

$$\eta_r = \frac{t\rho}{t_0\rho_0} \approx \frac{t}{t_0} \quad (9)$$

where t and t_0 are the flow times of the suspension and of the solvent respectively and ρ and ρ_0 are the densities of the suspension and the solvent respectively. Flow times were measured in triplicate with an Ubbelohde viscosimeter (Technico, 0.05 cSt s^{-1}) in air at $20 \text{ }^\circ\text{C}$. The flow time of water was estimated be $18.65 \pm 0.09 \text{ s}$ (measured five times in triplicate, $N = 15$). The intrinsic viscosity, and the Huggins coefficient, were extracted by fitting the relative viscosity as a function of the CNC concentration according to **Equation 4** and the 3D aspect ratio of the samples was estimated from the intrinsic viscosity by using **Equation 3**. The choice of approach and equation derivation are described in more detail in the Supporting Information.

Supporting Information

Supporting Information is available at the end of this document.

Acknowledgments

This work was funded by: EPSRC CDT, Automated Chemical Synthesis Enabled by Digital Molecular Technologies EP/S024220/1 (K.B., A.L.); EPSRC Bio-derived and Bio-inspired Advanced Materials for Sustainable Industries EP/W031019/1 (K.B., R.P., B.F.P., S.V.); EPSRC EP/T517847/1 (T.P.); ERC Horizon 2022 Proof of Concept Grants (ID: 101082172) (R.P., S.V.); Hiroshima University WPI-SKCM² (B.F.P.) This project was cofunded by European Regional Development Fund via the project “Innovation Centre in Digital Molecular

Technologies” (A.L.). JHL and YO acknowledge Agence Nationale de la Recherche (ANR grant number: ANR-21-CE29-0016-1) and Glyco@Alps (ANR-15-IDEX-02) for their financial support and the NanoBio-ICMG platform (FR 2607) for granting access to the electron microscopy facility. The authors would like to thank Dr. Heather Greer (University of Cambridge) for her general help in acquiring the TEM images (thanks to her EPSRC EP/P030467/1 grant). We also want to thank Nigel Howard (University of Cambridge) for the ICP-OES measurements.

References

- [1] R. F. Nickerson, J. A. Habrle, *Ind. Eng. Chem.* **1947**, *39*, 1507.
- [2] B. Frka-Petesic, T. G. Parton, C. Honorato-Rios, A. Narkevicius, K. Ballu, Q. Shen, Z. Lu, Y. Ogawa, J. S. Haataja, B. E. Droguet, R. M. Parker, S. Vignolini, *Chem. Rev.* **2023**, *123*, 12595.
- [3] S. J. Eichhorn, A. Etale, J. Wang, L. A. Berglund, Y. Li, Y. Cai, C. Chen, E. D. Cranston, M. A. Johns, Z. Fang, G. Li, L. Hu, M. Khandelwal, K.-Y. Lee, K. Oksman, S. Pinitsoontorn, F. Quero, A. Sebastian, M. M. Titirici, Z. Xu, S. Vignolini, B. Frka-Petesic, *J. Mater. Sci.* **2022**, *57*, 5697.
- [4] C. Schütz, J. R. Bruckner, C. Honorato-Rios, Z. Tosheva, M. Anyfantakis, J. P. F. Lagerwall, *Crystals* **2020**, *10*, 199.
- [5] S. Elazzouzi-Hafraoui, Y. Nishiyama, J.-L. Putaux, L. Heux, F. Dubreuil, C. Rochas, *Biomacromolecules* **2008**, *9*, 57.
- [6] T. G. Parton, R. M. Parker, G. T. van de Kerkhof, A. Narkevicius, J. S. Haataja, B. Frka-Petesic, S. Vignolini, *Nat Commun* **2022**, *13*, 2657.
- [7] O. M. Vanderfleet, E. D. Cranston, *Nat. Rev. Mater.* **2021**, *6*, 124.
- [8] Y. Tang, H. Yang, S. Vignolini, *Adv. Sustain. Syst.* **2022**, DOI 10.1002/adsu.202100100.
- [9] B. G. Rånby, *Discuss. Faraday Soc.* **1951**, *11*, 158.
- [10] A. Brinkmann, M. Chen, M. Couillard, Z. J. Jakubek, T. Leng, L. J. Johnston, *Langmuir* **2016**, *32*, 6105.
- [11] P. A. Buining, A. P. Philipse, H. N. W. Lekkerkerker, *Langmuir* **1994**, *10*, 2106.
- [12] Y. Boluk, L. Zhao, V. Incani, *Langmuir* **2012**, *28*, 6114.
- [13] H. Fukuzumi, R. Tanaka, T. Saito, A. Isogai, *Cellulose* **2014**, *21*, 1553.
- [14] F. Cherhal, F. Cousin, I. Capron, *Langmuir* **2015**, *31*, 5596.
- [15] F. Cherhal, B. Cathala, I. Capron, *Nord Pulp Paper Res J.* **2015**, *30*, 126.
- [16] T. Phan-Xuan, A. Thuresson, M. Skepö, A. Labrador, R. Bordes, A. Matic, *Cellulose* **2016**, *23*, 3653.
- [17] J. Meija, M. Bushell, M. Couillard, S. Beck, J. Bonevich, K. Cui, J. Foster, J. Will, D. Fox, W. Cho, M. Heidelmann, B. C. Park, Y. C. Park, L. Ren, L. Xu, A. B. Stefaniak, A. K. Knepp, R. Theissmann, H. Purwin, Z. Wang, N. de Val, L. J. Johnston, *Anal. Chem.* **2020**, *92*, 13434.
- [18] Y. Boluk, R. Lahiji, L. Zhao, M. T. McDermott, *Colloids Surf. A Physicochem.* **2011**, *377*, 297.
- [19] M. Doi, S. F. Edwards, *The Theory of Polymer Dynamics*, Clarendon Press., Oxford, **1986**.
- [20] H. Brenner, *Int. J. Multiph. Flow* **1974**, *1*, 195.
- [21] M. L. Huggins, *J. Am. Chem. Soc.* **1942**, *64*, 2716.

- [22] A. M. Wierenga, A. P. Philipse, *Colloids Surf. A Physicochem.* **1998**, *137*, 355.
- [23] E. González-Labrada, D. G. Gray, *Cellulose* **2012**, *19*, 1557.
- [24] R. Tanaka, T. Saito, H. Hondo, A. Isogai, *Biomacromolecules* **2015**, *16*, 2127.
- [25] Q. Wu, X. Li, Q. Li, S. Wang, Y. Luo, *Polymers* **2019**, *11*, 781.
- [26] Q. Wu, X. Li, S. Fu, Q. Li, S. Wang, *Cellulose* **2017**, *24*, 3255.
- [27] J. Li, J.-F. Revol, R. H. Marchessault, *J. Colloid Interface Sci.* **1996**, *183*, 365.
- [28] M. Martínez-Sanz, F. Pettolino, B. Flanagan, M. J. Gidley, E. P. Gilbert, *Carbohydr. Polym.* **2017**, *175*, 450.
- [29] W. Helbert, Y. Nishiyama, T. Okano, J. Sugiyama, *J. Struct. Biol.* **1998**, *124*, 42.
- [30] C. Bruel, S. Queffeuilou, P. J. Carreau, J. R. Tavares, M.-C. Heuzey, *Langmuir* **2020**, *36*, 12179.
- [31] F. Cherhal, F. Cousin, I. Capron, *Biomacromolecules* **2016**, *17*, 496.
- [32] I. Kalashnikova, H. Bizot, B. Cathala, I. Capron, *Biomacromolecules* **2012**, *13*, 267.
- [33] M. Uhlig, A. Fall, S. Wellert, M. Lehmann, S. Prévost, L. Wågberg, R. Von Klitzing, G. Nyström, *Langmuir* **2016**, *32*, 442.
- [34] C. Honorato-Rios, A. Kuhnhold, J. R. Bruckner, R. Dannert, T. Schilling, J. P. F. Lagerwall, *Front. Mater.* **2016**, *3*, 21.
- [35] S. Elazzouzi-Hafraoui, J.-L. Putaux, L. Heux, *J. Phys. Chem. B* **2009**, *113*, 11069.
- [36] S. Kratochvil, G. E. Janauer, E. Matijević, *J. Colloid Interface Sci.* **1969**, *29*, 187.
- [37] M. Chau, S. E. Sriskandha, D. Pichugin, H. Thérien-Aubin, D. Nykypanchuk, G. Chauve, M. Méthot, J. Bouchard, O. Gang, E. Kumacheva, *Biomacromolecules* **2015**, *16*, 2455.
- [38] G. Lenfant, M.-C. Heuzey, T. G. M. van de Ven, P. J. Carreau, *Rheol Acta* **2017**, *56*, 51.
- [39] M. S. Reid, S. A. Kedzior, M. Villalobos, E. D. Cranston, *Langmuir* **2017**, *33*, 7403.
- [40] I. Capron, O. J. Rojas, R. Bordes, *Curr. Opin. Colloid Interface Sci.* **2017**, *29*, 83.
- [41] Z. Hao, W. Y. Hamad, P. Yaseneva, *J. Chem. Eng.* **2023**, *478*, 147160.
- [42] T. Wagner, H.-G. Lipinski, *J. Open Res. Softw.* **2013**, *1*, e6.
- [43] R. F. Fedors, *Polymer* **1979**, *20*, 225.
- [44] M. Bercea, P. Navard, *Macromolecules* **2000**, *33*, 6011.
- [45] G. Lenfant, M. C. Heuzey, T. G. M. van de Ven, P. J. Carreau, *Cellulose* **2015**, *22*, 1109.
- [46] M.-C. Li, Q. Wu, R. J. Moon, M. A. Hubbe, M. J. Bortner, *Adv. Mater.* **2021**, *33*, 2006052.

Supporting Information

Directed Aggregation of Cellulose Nanocrystals to Enhance Chiral Twist

Kévin Ballu, Jia-Hui Lim, Thomas G. Parton, Richard M. Parker, Bruno Frka-Petesic, Alexei A. Lapkin, Yu Ogawa, Silvia Vignolini**

Kévin Ballu, Dr Richard M Parker, Dr Bruno Frka-Petesic
Yusuf Hamied Department of Chemistry, University of Cambridge, Cambridge CB2 1EW, United Kingdom

Jia-Hui Lim, Dr Yu Ogawa
Univ. Grenoble Alpes, CNRS, CERMAV, 38000 Grenoble, France
* E-mail: yu.ogawa@cermav.cnrs.fr

Dr Thomas G Parton, Prof Silvia Vignolini
Department of Sustainable and Bio-inspired Materials, Max Planck Institute of Colloids and Interfaces, 14476 Potsdam, Germany
* E-mail: sv@mpikg.mpg.de

Dr Bruno Frka-Petesic
International Institute for Sustainability with Knotted Chiral Meta Matter (WPI-SKCM²), Hiroshima University, Hiroshima 739-8526, Japan

Prof Alexei Lapkin
Department of Chemical Engineering and Biotechnology, Philippa Fawcett Drive, Cambridge CB3 0AS, United Kingdom

Prof Alexei Lapkin
Innovative Center in Digital Molecular Technologies, Yusuf Hamied Department of Chemistry, University of Cambridge, Cambridge CB2 1EW, United Kingdom

SI.1. TEM and Cryo-TEM analysis

SI.1.1 TEM Images and Size Distributions

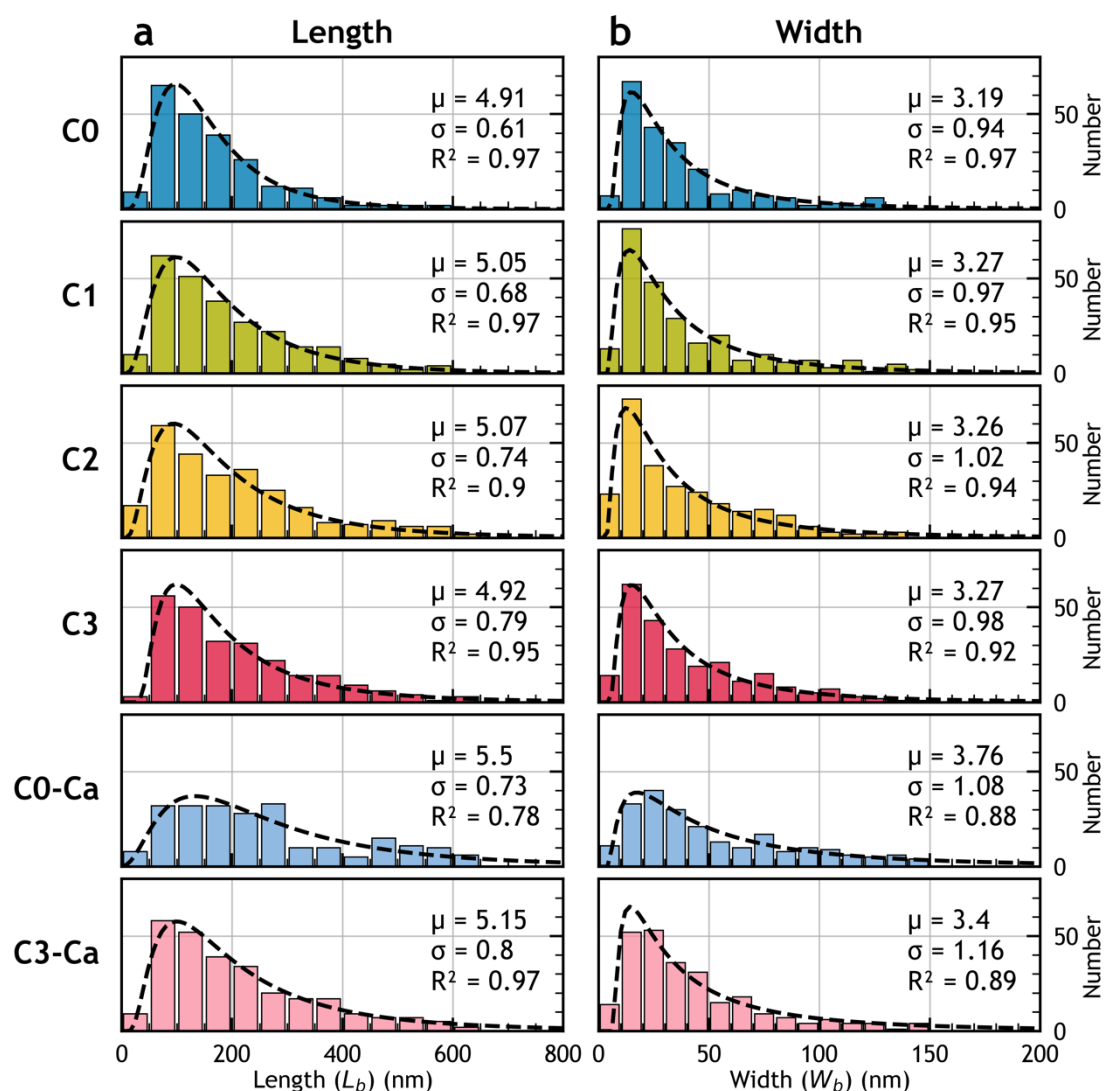


Figure S1. Histograms of CNC (a) bounding box lengths (L_b) and (b) bounding box widths (W_b) from the TEM measurements of CNCs that were never centrifuged (C0), or standard CNCs (C1-3), and of the calcium-aggregated CNCs prepared from never centrifuged (C0-Ca) and centrifuged three times CNCs (C3-Ca). The data was fitted with a log-normal distribution and the corresponding fitting parameters are presented for each plot.

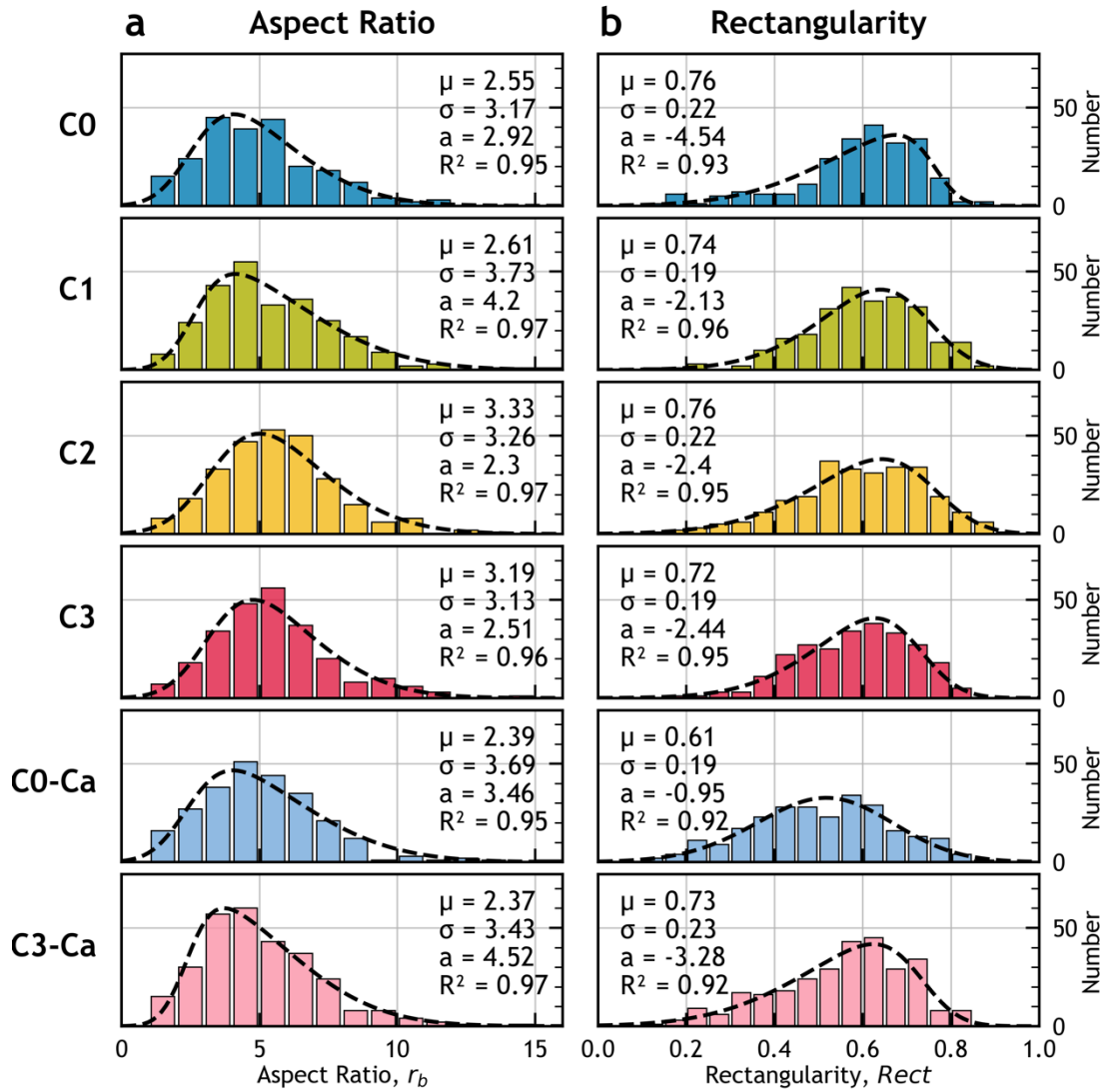


Figure S2. Histograms of CNC (a) bounding box aspect ratio (r_b) and (b) rectangularity ($Rect$) calculated from the TEM images of CNCs that were never centrifuged (C0), or standard CNCs (C1-3), and of the calcium-aggregated CNCs prepared from never centrifuged (C0-Ca) and centrifuged three times CNCs (C3-Ca). The data was fitted by skewed-normal distributions, the corresponding fitting parameters are presented for each plot.

SI.1.2 Statistical Analysis of TEM Values

The normality of the values obtained from TEM analysis was analyzed by applying a Shapiro-Wilk test on the logarithm of the bounding box lengths (L_b) and bounding box widths (W_b) and directly (without transformation of the data) on the corresponding bounding box aspect ratios (r_b) and rectangularities ($Rect$). As presented in **Table S1**, most series did not follow a normal distribution with a confidence threshold of 0.05. Consequently, sample distributions were compared by using a Mann-Whitney U test, as it does not assume normality.

Table S1. P-values from the Shapiro-Wilk test of normality for the logarithm of the bounding box lengths (L_b) and widths (W_b) and for the corresponding aspect ratio (r_b) and rectangularity (**Rect**) for each sample. A p-value < 0.05, highlighted by a grey color, indicates that the data is not normally distributed.

Sample	$\ln(L_b)$	$\ln(W_b)$	r_b	Rect
C0	0.346	0.001	0.000	0.000
C1	0.155	0.000	0.000	0.004
C2	0.005	0.002	0.000	0.003
C3	0.003	0.007	0.000	0.008
C0-Ca	0.021	0.073	0.000	0.190
C3-Ca	0.871	0.000	0.000	0.000

SI.1.3 Typical Images from Cryo-TEM

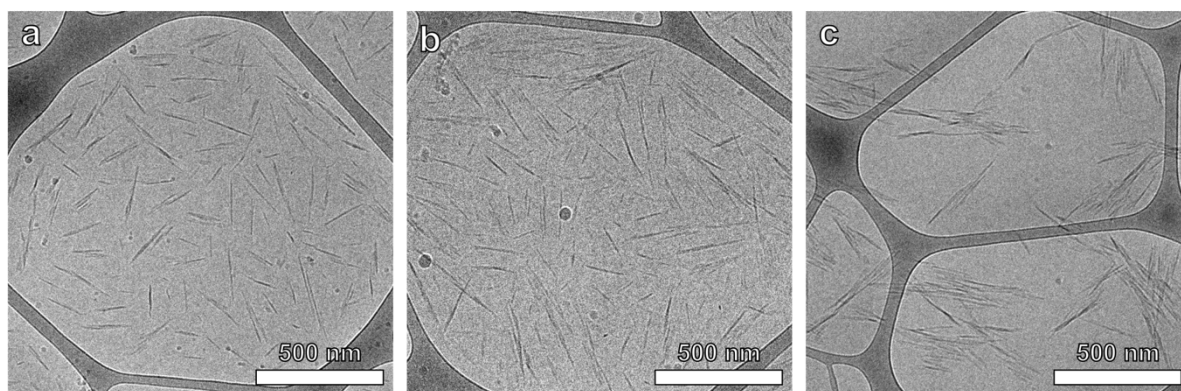


Figure S3. Typical images from Cryo-TEM of (a) never centrifuged CNCs (**C0**), (b) standard CNCs (**C3**) and (c) salt aggregated CNCs (**C3B**).

SI.2. Viscosity Measurements

SI.2.1 Fitting of the Relative viscosity

In most previous studies, the intrinsic viscosity of a CNC suspension was obtained by fitting the data using a Fedors plot, according to the following expression:^[18,23–26,43,44]

$$\frac{1}{2(\sqrt{\eta_r} - 1)} = \frac{1}{[\eta]c} - \frac{1}{[\eta]c_m} \quad (10)$$

where η_r and $[\eta]$ are respectively the relative and intrinsic viscosities, and c and c_m are respectively the particle concentration and the concentration at maximum packing. However, this approach often yields physically incoherent (negative) critical concentrations,^[45] which was also the case for our data, as illustrated in **Figure S4** and **Table S2**. This might be because this approach relies on the following expression:

$$\eta_r = \left(1 + \frac{1.25\varphi}{1 - \frac{\varphi}{\varphi_m}} \right)^2 \quad (11)$$

where φ and φ_m are the particle volume fraction and volume fraction at maximum packing respectively. Therefore, we recommend using the Huggins approach, presented in **Equation 4**, which does not rely on such an assumption.

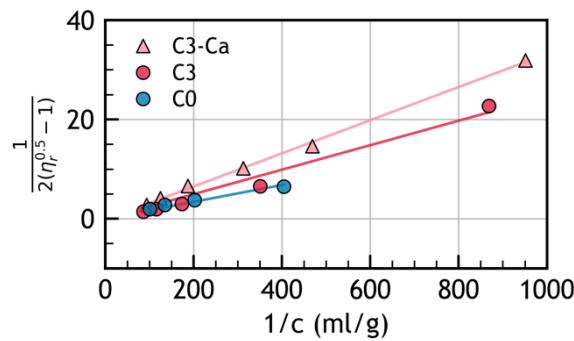


Figure S4. Fedors plot of the relative viscosity data. Note that values above 0.001 g mL⁻¹ were excluded, as recommended by the author of the method.

Table S2. Results from the Fedors fit

Sample	$[\eta]$ (mL g ⁻¹)	c_m (g mL ⁻¹)	R ²
C0	59.0 ± 8.1	41198 ± 5.6E+10	0.95
C3	40.6 ± 4.6	-37105 ± 6.6E+10	0.97
C3-Ca	29.9 ± 0.7	0.2 ± 0.3	1.00

Table S3. Results from the Huggins fit

Sample	$[\eta]$ (mL g ⁻¹)	K_H	R^2
C0	56 ± 6	0.1 ± 0.2	0.99
C3	54 ± 2	0.5 ± 0.1	1.00
C3-Ca	25 ± 3	1.6 ± 0.8	0.99

SI.2.2 Expression for 3D Aspect Ratio

Various expressions for rods and spheroids can be used to relate the 3D aspect ratio to the intrinsic viscosity, the Simha relation being the most widespread.^[46] However, this expression is specific to rods and the CNC bundles in this work are closer in shape to a spheroid than a cylinder. Therefore, it seemed more appropriate to use an expression derived from Doi and Edwards, and Brenner for prolate spheroids,^[19,20] for which the rotational friction constant is exactly resolved.

The intrinsic viscosity is defined as:

$$[\eta] = \lim_{c \rightarrow 0} \frac{1}{c} \frac{\eta - \eta_s}{\eta_s} \quad (12)$$

where η and η_s are the viscosities of the polymer and of the solvent respectively. In steady shear flow rate for rod-like polymers, the viscosity can be expressed as:^[19]

$$\eta = \eta_s + \frac{2}{15} \frac{c}{\rho_p V_p} \zeta_{rot} \quad (13)$$

where c is the particle concentration, ρ_p is the particle density, V_p is the volume of a particle, and ζ_{rot} is their rotational friction constant. According to Brenner,^[20] the rotational friction constant can be expressed as:

$$\zeta_{rot} = \eta_s 6V_p K \quad (14)$$

where K is a dimensionless scalar coefficient defined in **Equation 16**. Consequently, from **Equation 12-14**, the intrinsic viscosity can be simplified as:

$$[\eta] = \frac{4}{5} \frac{K}{\rho_{CNC}} \quad (15)$$

For spheroids:^[20]

$$K = \frac{2(r_{3D}^2 + 1)}{3(r_{3D}^2 \alpha_{\parallel} + \alpha_{\perp})} \quad (16)$$

with:

$$\alpha_{\perp} = \frac{r_{3D}^2}{r_{3D}^2 - 1} (1 - \beta) \quad (17)$$

$$\alpha_{\parallel} = \frac{2}{r_{3D}^2 - 1} (r_{3D}^2 \beta - 1) \quad (18)$$

and where r_{3D} , the 3D aspect ratio of the spheroid, is expressed as:

$$r_{3D} = \frac{L}{d} \quad (19)$$

with L and d the long and small axes, respectively. Finally, for prolate spheroids ($r_{3D} > 1$):

$$\beta = \frac{\cosh^{-1}(r_{3D})}{r_{3D}(r_{3D}^2 - 1)^{\frac{1}{2}}} \quad (20)$$

Finally, this yields **Equation 3** presented in the Results and Discussion section 2.2.

SI.3. Microelectron Diffraction

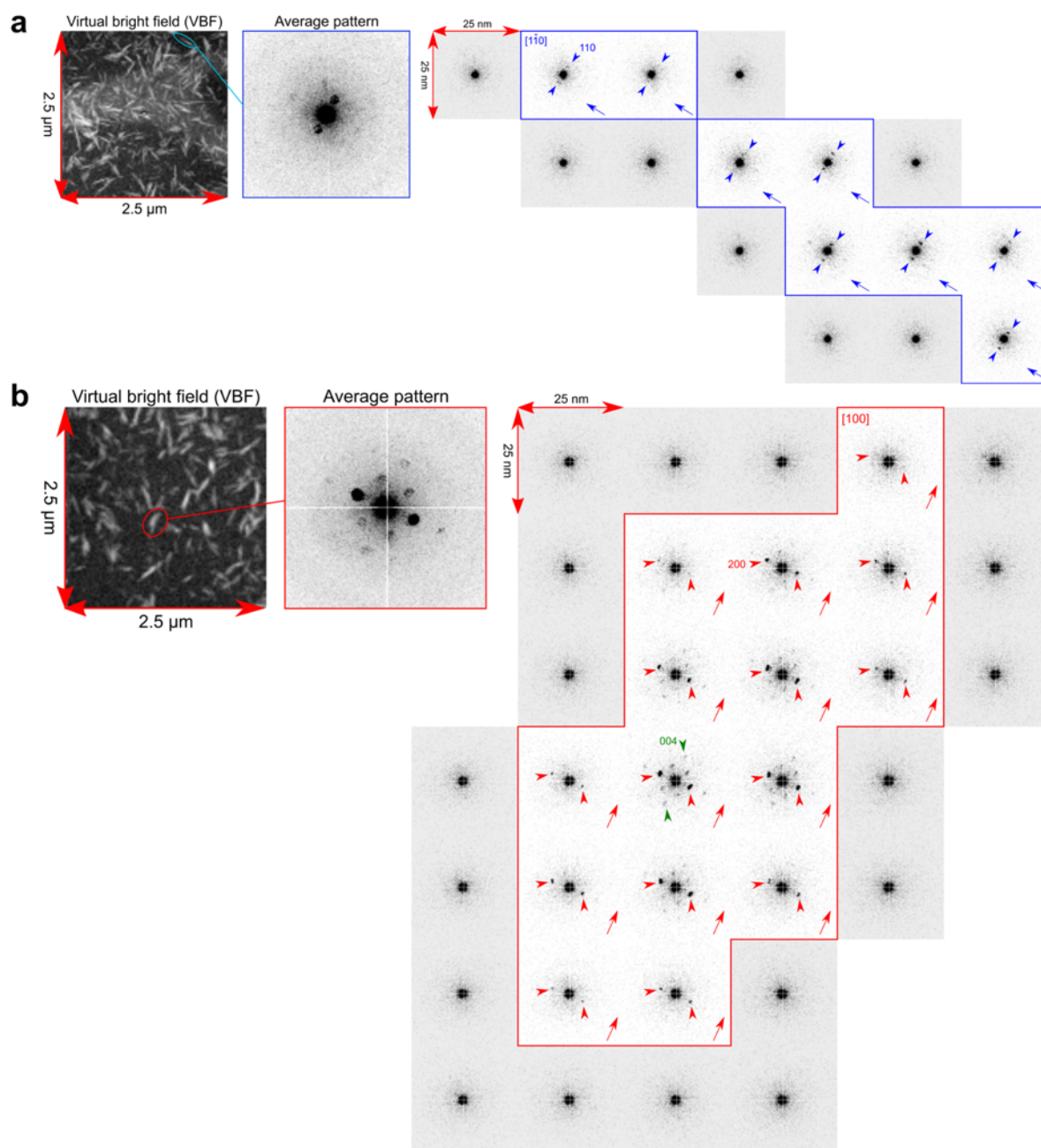


Figure S5. SNBED analysis with virtual bright field image (left), average diffraction pattern and ED patterns along a CNC for (a) a never-centrifuged CNC (C0) displaying a [1-10] zone axis and (b) a standard CNC (C3) displaying a [100] zone axis. The arrows on the corner of each ED pattern indicate the fiber axis.

SI.4. Self-organization of C3-Ca

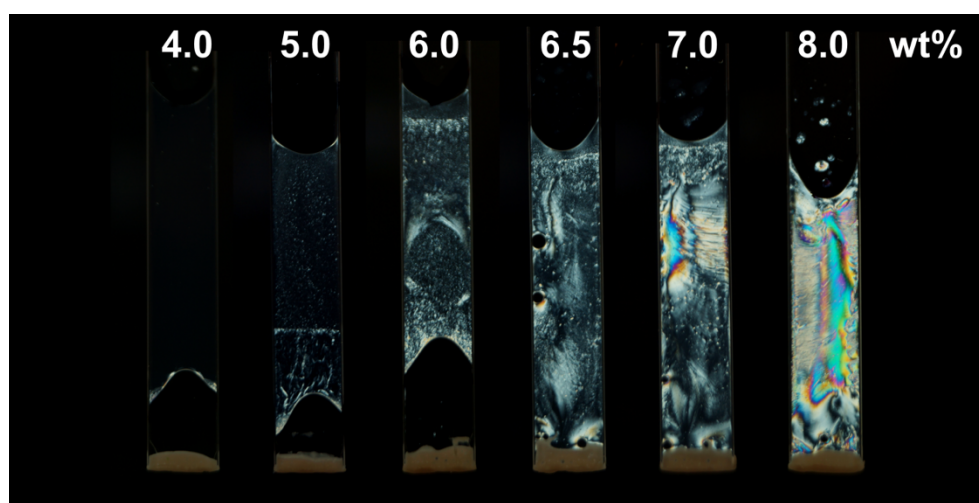


Figure S6. Photograph of a series of capillaries containing calcium-CNC (Ca-C3) suspensions with increasing volume fractions.

SI.5. CNC Surface Properties

Table S4. Summary of CNCs surface characteristics: ζ -potential, surface charge per CNC mass (b_{charge}) from titration measurements, and calcium content from elemental analysis.

Sample	ζ -potential (mV)	b_{charge} (mmol kg ⁻¹)	Ca content (mmol kg ⁻¹)
C0	-48 ± 5	264 ± 5	-
C1	-50 ± 8	269 ± 5	-
C2	-49 ± 5	267 ± 5	-
C3	-50 ± 8	264 ± 5	6
C0-Ca	-36 ± 1	-	-
C3-Ca	-34 ± 2	-	133

SI.6. Fitting the Hydrodynamic Diameter as a Function of Ultrasonication Dose

By relating the size change to a simple dissociation reaction, one can express an infinitesimal change of size (dD) as a function of an infinitesimal change of ultrasonication dose (du_s) by using the rate equation:

$$\frac{dD}{du_s} = -k * D \quad (21)$$

where Z is the size and k is the rate of size change. This differential equation can be integrated into:

$$D(u_s) = [D(0) - D_\infty] * \exp(-k * u_s) + D_\infty \quad (22)$$

Considering that the dissociation of the calcium objects occurs independently of the standard CNCs, one can add a second term to express the size change of CaCl_2 aggregated objects:

$$D^{\text{Ca}}(u_s) = [D^{\text{Ca}}(0) - D(0)] * \exp(-k^{\text{Ca}} * u_s) + [D(0) - D_\infty] * \exp(-k * u_s) + D_\infty \quad (23)$$

which is equivalent to:

$$D^{\text{Ca}}(u_s) = [D^{\text{Ca}}(0) - D(0)] * \exp(k^{\text{Ca}} * u_s) + D(u_s) \quad (24)$$

Using this simple approach, we extracted the rate of dissociation for the standard CNCs and reused them to fit their calcium versions, as illustrated in **Figure S7**. This approach leads to a reasonably good fitting of the data, as indicated by the high R^2 and low MSE presented in **Table S5**, but the model misses some features at intermediate ultrasonication doses. To improve the description of the experimental observations while keeping a physically meaningful model, we introduced a stretch coefficient α in the dissociation rate to get **Equation 6**.

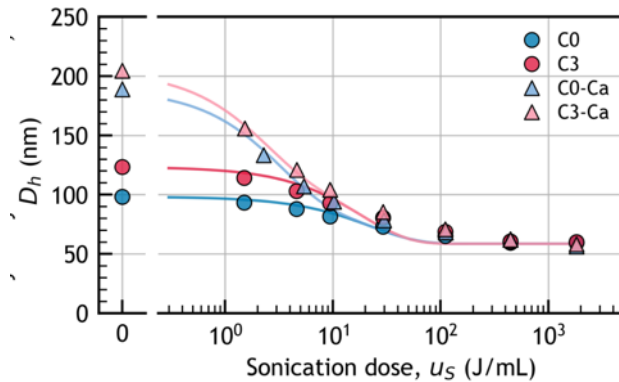


Figure S7. Evolution of the hydrodynamic diameter (D_h) as a function of the sonication dose (u_s) and best fit using **Equations 22 & 23**. With **C0** (blue circles), **C3** (red circles), **C0-Ca** (blue triangles), and **C3-Ca** (red triangles).

Table S5. Best fitting parameter (k) and goodness of fit (R^2 and MSE) for the evolution of the hydrodynamic diameter as a function of the sonication dose using a simple dissociation function (Equations 22 & 23).

Sample	k (mL L ⁻¹)	R^2	MSE
C0	0.044 ± 0.008	0.95	9.9
C3	0.054 ± 0.01	0.94	32.4
C0-Ca	0.33 ± 0.05	0.98	32.6
C3-Ca	0.46 ± 0.1	0.98	48.3

Table S6. Best fitting parameters (k and α) and goodness of fit (R^2 and MSE) for the evolution of the hydrodynamic diameter as a function of the sonication dose using a modified dissociation function (Equations 7 & 8).

Sample	k (mL L ⁻¹)	α	R^2	MSE
C0	0.030 ± 0.003	0.57 ± 0.04	1.00	1.0
C3	0.036 ± 0.004	0.53 ± 0.04	0.99	3.5
C0-Ca	0.30 ± 0.03	0.66 ± 0.09	1.00	6.4
C3-Ca	0.34 ± 0.03	0.74 ± 0.09	1.00	5.2

SI.7. Influence of process parameters on the size of aggregated CNCs

Table S7. Impact of the aggregation time (t_{agg}) and number of centrifugation cycles (N_{centri}) on the hydrodynamic diameter (D_h) of diluted CNCs after salt-induced aggregation of **C3** at 6.49wt% CNC and 51.4 mM of ionic strength induced by $CaCl_2$ addition.

Entry	t_{agg}	N_{centri}	D_h (nm)
A	0 h		209 ± 1
B	1 h		293 ± 2
C	3 h	0	299 ± 4
D	24 h		270 ± 2
E	196 h		275 ± 3
F	/	1	285 ± 5
G	/	2	274 ± 2
H	50 days	1	274 ± 6

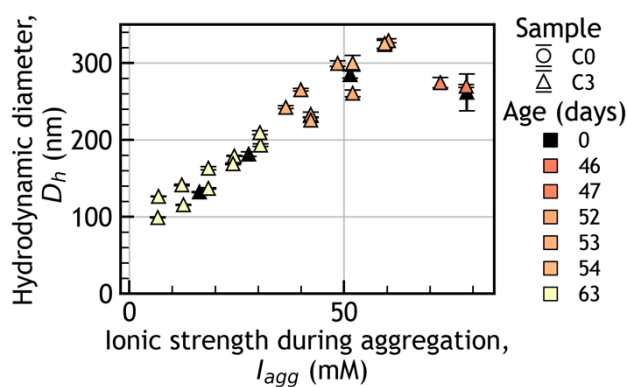


Figure S8. Evolution of the CNC hydrodynamic diameter after dilution following $CaCl_2$ induced aggregation as a function of ionic strength (I_{agg}), CNC sample, and waiting time before dilution.